GJI Geodynamics and tectonics

First evidences of fast creeping on a long-lasting quiescent earthquake normal-fault in the Mediterranean

Roberto Sabadini,[1] Abdelkrim Aoudia,[2] Riccardo Barzaghi,[3] Bruno Crippa,[1] Anna Maria Marotta,[1] Alessandra Borghi,[4] Letizia Cannizzaro,[3] Laura Calcagni,[1] Giorgio Dalla Via,[1] Grazia Rossi,[1] Raffaele Splendore[1] and Michele Crosetto[5]

[1] *Section of Geophysics, Department of Earth Sciences "A. Desio", Università degli Studi di Milano, Via L. Cicognara 7, 20129 Milano, Italy. E-mail: roberto.sabadini@unimi.it*

[2] *Earth System Physics Section, International Centre for Theoretical Physics, Strada Costiera 11, 34014 Trieste, Italy*

[3] *DIIAR, Department of Environmental, Hydraulic, Infrastructures and Surveying Engineering Politecnico di Milano, P.zza Leonardo da Vinci 32, 20133 Milano, Italy*

[4] *OGS-National Institute of Oceanography and Experimental Geophysics, c/o Politecnico di Milano, P.zza Leonardo da Vinci 32, 20133 Milano, Italy*

[5] *Institute of Geomatics, Avinguda del Canal Olimpic, E-08860 Castelldefels, Barcelona, Spain*

SUMMARY

A key issue in our understanding of the earthquake cycle and seismic hazard is the behaviour of an active fault during the interseismic phase. Locked and creeping faults represent two end-members of mechanical behaviours that are given two extreme rupturing hazard levels, that is, high and low, respectively. Geophysical and space geodetic analyses are carried out over the Pollino Range, an extensional environment within the Africa–Eurasia plate boundary, to disclose the behaviour of the long-lasting quiescent Castrovillari normal fault. Fault trenching evidenced at least four large earthquakes (6.5–7.0 M_w) in the past and an elapsed time of 1200 yr since the last event. Inversion of Differential Interferometric Synthetic Aperture Radar and Global Positioning System over a decade shows fast creeping at all depths of the fault plane. The velocity-strengthening creeping zone reaches maximum rates 20 mm yr^{-1} against an average rate of about 3–9 mm yr^{-1}. It limits the southern-weakening locked part of the fault. An essential condition for the generation of a large earthquake on the Castrovillari fault, as has occurred in the past, is a rupture through the velocity-strengthening zone. The Castrovillari fault yields the best evidence for being both a strong and weak fault during its earthquake cycle. Creeping at rates faster than its tectonically driven ones, it must thus consist of a mix of unstable and conditionally stable patches ready to sustain a sizeable earthquake. Quantifying and mapping the slip rate over the fault plane is important because they influence fault moment budget estimate and helps to constrain constitutive laws of fault zones. Aseismic slip also redistributes stress in the crust, thereby affecting the locations of future earthquakes.

Key words: Space geodetic surveys; Earthquake source observations; Dynamics; seismotectonics.

1 INTRODUCTION

We evaluate a comprehensive stack of 1995–2000 51 ERS interferograms and GPS campaign velocities spanning 2003–2008 to survey vertical and horizontal motions over the Castrovillari normal-fault, in the Southern Apennines (Italy), in order to characterize its behaviour over the as long as possible time interval allowed by geodetic techniques.

Differential Interferometric Synthetic Aperture Radar (DInSAR) and Global Positioning System (GPS) techniques, together with geophysical modelling, make it possible to monitor and model Earth's deformation at different lengths and timescales. Forward geophys-

ical models, at the regional scale of tectonic processes and at the local scale of active faults, used in conjunction with the pertinent geodetic data allow for a rigorously deterministic description of the earthquake cycle. Such an integrated geophysical and geodetic approach is brought to bear on the slowly deforming, normal faulting Pollino–Castrovillari quiescent and seismogenic zone (Cinti *et al.* 2002), the most prominent seismicity gap in Italy (Camassi & Stucchi 1997). Deformation rates are sampled from that characterizing long-timescale tectonic processes to the ones of the fault, from the observational and modelling standpoint, zooming therefore both in space and time. At short time and length scales DInSAR and GPS campaign data around the Castrovillari fault are thus analysed:

SAR images and GPS data make possible a decade time-interval coverage. This is a sufficiently long span to detect vertical and horizontal velocities by combining vertical DInSAR and horizontal GPS surface measurements.

Attention is drawn herein to an active but slowly extensional deforming zone, struck by shallow, normal fault earthquakes, within the diffuse plate boundary between Africa and Eurasia.

Our study on the inter- and pre-seismic phase of the Castrovillari fault deals with the behaviour of active faults, which can remain locked or slip aseismically, in a mode named fault creep. The latter has been discovered by some pioneering works on strike-slip faults, the San Andreas in California and the North Anatolian Fault in the Mediterranean, in the last 50 yr (Steinbrugge *et al.* 1960; Ambraseys 1970; Bürgmann *et al.* 1998, 2000; Rosen *et al.* 1998; Cakir *et al.* 2005). It has been shown that creep occurs at different spatial and timescales, involving various depths within the seismogenic layer, at rates which may be different with respect to the background tectonic ones. Fault creep patterns, including the intensity of creep, provide major information on the earthquake cycle, being the mode of stress accumulation leading to earthquakes dependent on the interplay between creeping and locked parts of the fault. Our analysis allows us to address such issues for normal faulting, and thus to verify whether creep is a general phenomenon occurring over all classes of active faults, not limited to strike-slip ones. Previous works on creep for the San Andreas and North Anatolian faults have also taken advantage of DInSAR and GPS technologies, but it is the first time in our analysis that such data are exploited within a generally slowly deforming plate boundary.

2 DInSAR ANALYSIS

SAR images cover the time interval after the 1993–1995 gap in ERS1 data and before ERS1 completed its mission, with ERS2 operating in gyroless mode in 2001.

The data set consists of 38 images taken in the 1995–2000 interval, by means of which 51 differential interferograms have been formed, based on a DEM obtained from aerophotogrammetry with a 25 m step; 40×8 multilooks have been used, that is, pixels having an approximate footprint of 160 m $\times$ 160 m; the accuracy of this DEM is around a few meters. In order to form a stack of interferograms, the threshold for temporal and perpendicular baselines are, respectively, fixed at 600 d and 300 m. In Tables S1 and S2, the parameters of the interferogram stack used for the analysis are reported, in terms of temporal and perpendicular baselines: from all possible couples forming the images, interferograms are selected in terms of the value of temporal and perpendicular baselines.

From geometry acquisition of ERS1/2 we are able to detect only the LOS component of deformation, generally representing the vertical displacement. The EW displacement contribution could be recovered using ascending and descending orbits and estimating two LOS for each coherent pixel in both stack interferograms. However, the low deformation rate and the decrement in the number of coherence pixels in the two stack interferograms, lead us to not try to apply the separation, in agreement with Wright *et al.* (2004). In addition, the estimate of the EW component, in a process, which has a prevalent vertical displacement, could introduce a disturbing element. We are conscious that the estimated vertical displacement could be slightly overestimated, with errors of around 1 mm yr^{-1}.

Since the areas of medium-high coherence are very clustered and far from each other, as shown by the white regions of high coherence in Fig. 1, rather than considering the full frame of interferograms,

we preferred to concentrate our analysis on the area in which the geological survey observations mapped the normal fault (Cinti *et al.* 2002). The geometry of the mapped fault does not mimic the structure of a classical intermountain basin (Bousquet 1973) and to our knowledge no evidence, in the area, of subsidence due to water level changes are reported.

DInSAR vertical rates are shown in Fig. 2, where the colour scale ranges from the largest subsidence of -6 to -2 mm yr^{-1} (blue) to the highest uplift of 4–7 mm yr^{-1} (red). These vertical rates are derived from an interferograms stack applying an advanced DInSAR procedure separating the linear deformation component of the observed interferometric phases from other contributions such as the topographic and atmospheric contributions, including orbital effects and phase noise (Biescas *et al.* 2007). The rates were estimated only over the pixels showing high coherence in the entire stack of processed interferograms. A broad subsidence overprints the surface projection of the hanging wall of the Castrovillari fault, whose right-hand border corresponds to the northwest–southeast trending thin line depicting the fault scarps (Cinti *et al.* 2002); uplift stands over the footwall, in agreement with normal fault-like motion.

3 CAMPAIGN GPS NETWORK ANALYSIS

Although Calabria (Southern Italy) is located in the Africa–Eurasia plate boundary, only few permanent GNSS stations have been set up in this zone and no available GNSS stations are present over the Castrovillari fault.

In order to disclose the behaviour of the long-lasting quiescent Castrovillari normal fault, a campaign GPS network composed by 10 sites over an area of about 30 km $\times$ 17 km has thus been set up, centred in the normal-faulting area (Figs 1 and 2). Implementation of the campaign sites was carefully performed to ensure a submillimetre forced centring. The GPS measurements started in 2003 and five campaigns have been performed up to 2008. During each campaign, data were collected over a period of four consecutive days, with daily sessions of at least 8 hr; some network sites have been observed continuously.

Data analysis makes use of the Bernese Software v.5.0 (Dach *et al.* 2007) selecting the Quasi Iono Free (QIF) strategy for ambiguity fixing. Tropospheric parameters were estimated on hourly basis and wet delays were modelled as stochastic parameters, using the Dry_Niell mapping function. The ionospheric disturbance has been treated using global ionospheric models by CODE (Hugenobler *et al.* 2000) in the L1 and L2 ambiguity estimation step and using the iono-free observations (L3) in the coordinate computation. Absolute phase centre variation (PCV) parameters have been used both for receiver and satellite antennas, according to the International GNSS Service (IGS) standard. The daily coordinate solutions have been computed in the reference frame coherent with the IGS precise orbits, using the IGS stations WTZR, ZIMM, MATE, GRAS, CAGL, NOT1 and GRAZ, depending on the current reference frame realization. Station coordinates have been framed in IGS05 using the IGS transformation parameters at the end of the processing analysis. Furthermore, data have been reduced for the common mode error (CME), estimated as a common daily bias in the observations (Widowinski *et al.* 1997) A single bias model seems to be a reasonable assumption due to the limited extension of the investigated area. By subtracting the CME from the daily coordinates, the horizontal repeatability of the coordinates improves from 2.4 to 1.1 mm.
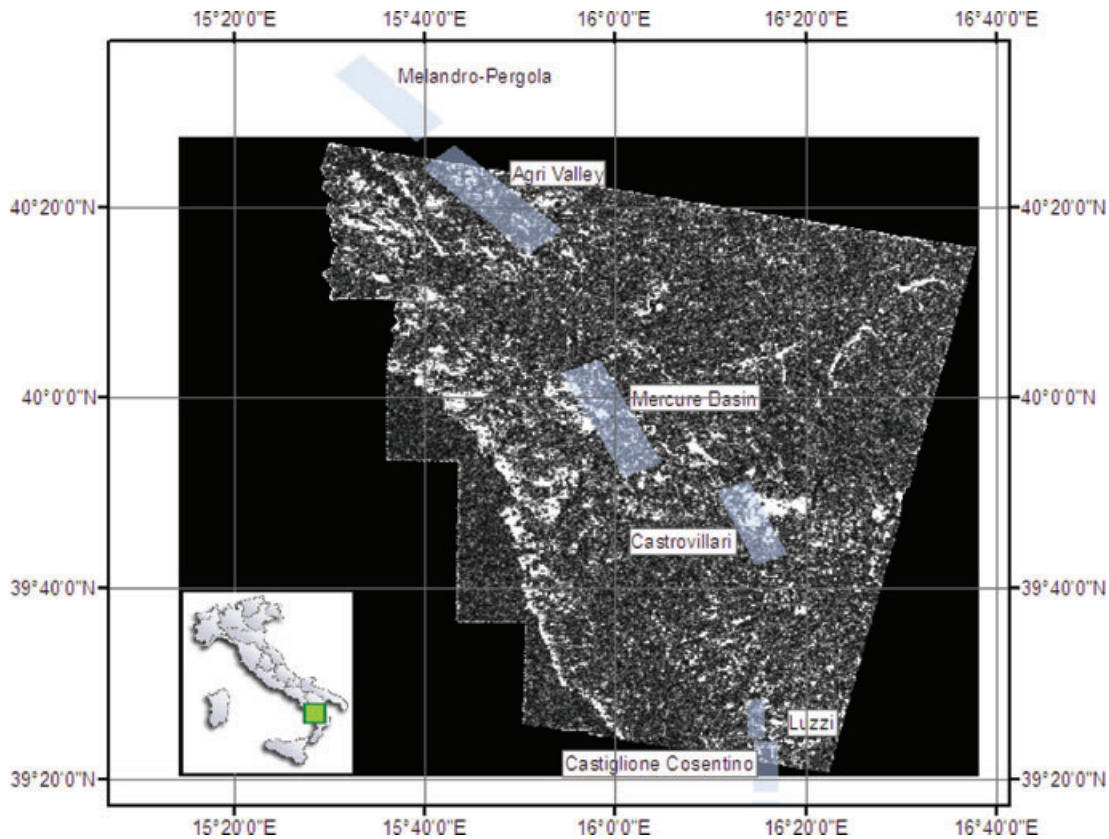
Figure 1. Example of the coherence image, 40 × 8 azimuth range multilook; the DInSAR analysis has been performed over the area overprinting the Castrovillari fault. Nearby active normal faults in the southern Apennines are also shown (redrawn from the Database of Individual Seismogenic Sources, DISS Working Group 2007). All the faults are characterized by a dip angle of 60.0°, except Luzzi, where this parameter is fixed at 65.0°. See DISS (DISS Working Group 2007), for more details. The inset shows the location of the coherence image in peninsular Italy.

For each site, velocities were computed by fitting a linear model in the 20-daily solutions, distributed from 2003 September to 2008 September (see Fig. S1 and Table S3); although more complex models are used to fit GNSS permanent station time-series (e.g. Nikolaidis 2002; Amiri-Simkooei 2007), this seems to be the most feasible model for the collected data (five campaigns for an amount of twenty coordinates). Furthermore, we note that the campaigns, except for the 2004 one, have been carried out in the same period (September–October).

The computed velocities, after datum shift to ITRF2005, were computed with respect to the Eurasia reference frame using the APKIM2005 model (Drewes 2006).

The GPS velocity field in the Eurasia reference frame, Fig. 3 and Table 1, shows significantly non-zero velocities (at significance level $\alpha = 1$ per cent) and a different behaviour across the fault. The velocity vectors of the sites in the footwall ('dorm', 'civi', 'cass' and 'fran') differ, both in magnitude and direction, from those in the hanging wall ('colo', 'mora', 'croc', 'zacc', 'dolc' and 'fras').

Assuming an homogeneous deformation field, the horizontal strain-rates have been computed via a least-square approach using the GPS velocities of each site. The east component of the 'civi' station (27.1 ± 0.5 mm yr^{-1}) is notably higher than the mean east velocity of the other station (23.8 ± 1.2 mm yr^{-1}). The statistical test on normal residuals has confirmed this anomalous behaviour and proved that the east velocity component of 'civi' has to be considered as an outlier. Hence, this network point has been removed

from the horizontal strain-rate estimate. The horizontal principal strain rate axes show an extension perpendicular to the strike of the fault (Table 2 and Fig. 4a), whose surface signature is provided in panel a by its scarps, in agreement with normal faulting.

Measured strain-rates of Fig. 4(a) can be compared with modelled strain-rates at tectonic regional scales, according to Marotta *et al.* (2004), based on thin-sheet modelling and ITRF2005 Africa–Eurasia relative motion (ITRF2005 2005). As continuous GPS data surrounding the Castrovillari fault are not available, we in fact make use of tectonic finite element modelling to zoom into the Pollino Range, indicated by the thin square in Fig. 4(b). This makes it possible to verify whether the extension perpendicular to the fault, as in Fig. 4(a), is coherent with tectonic strain-rates. That this is the case is shown by the outward arrows indicating strain-rates in terms of eigenvalues and eigenvectors, evaluated from the finite element model, following the procedure described in Marotta & Sabadini (2004), providing an extension of 5 nanostrain yr^{-1}. This extension at the regional scale of the Pollino range is fully concordant with that of 3–6 nanostrain yr^{-1} from continuous (2001–2006) GPS, grey arrows, and from global scale modelling (Fig. 4c), black arrows, within the NOTO-MATE-AQUI triangle, evaluated as for the strain-rates of Fig. 4(b). Noteworthy is that strain rates at the local scale of the characteristic fault dimension are one order of magnitude higher than those acting at the regional scale and at the scale of the central Mediterranean (e.g. Battaglia *et al.* 2004).
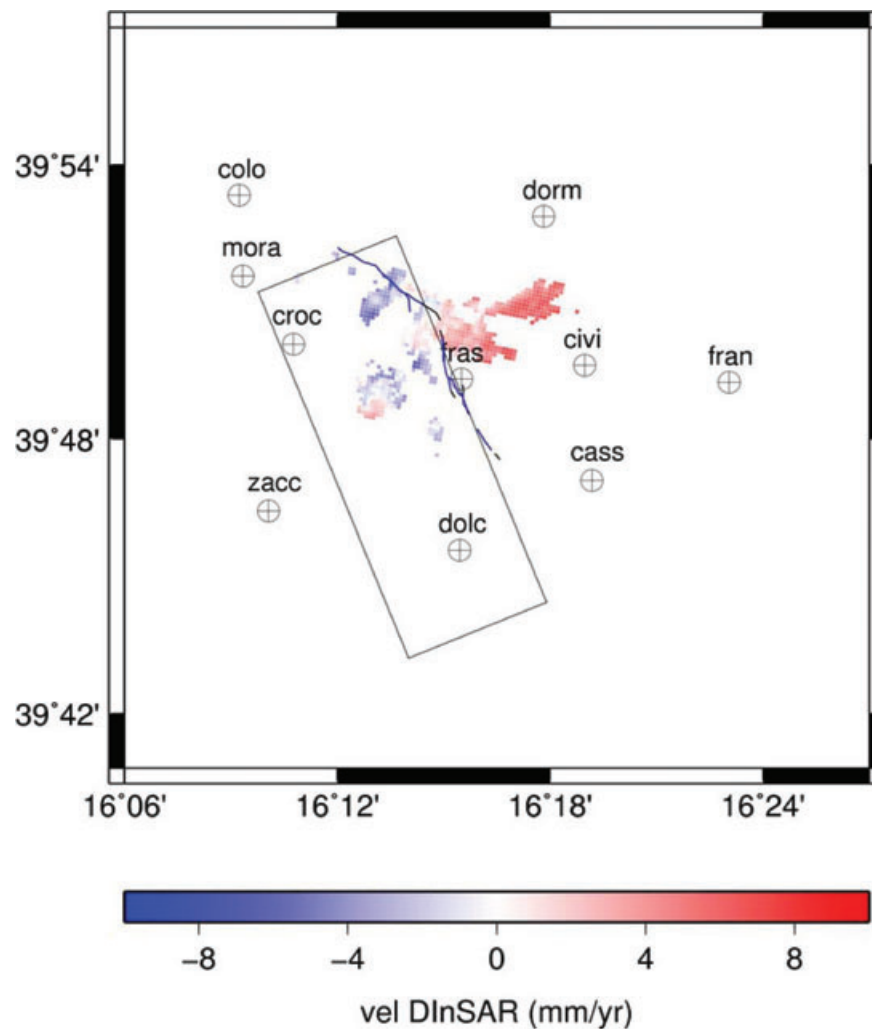
Figure 2. DInSAR vertical velocity from SAR images covering the period 1995–2000. Each pixel represents the unit of the SAR image, containing information on the amplitude and phase of the reflected radar signal. The surface projection of the Castrovillari normal fault is depicted by the rectangle, with the blue line indicating the fault scarps, from Cinti *et al.* (2002). GPS sites are also shown.

4 DATA INTERPRETATION AND MODELLING

Vertical and horizontal velocities are considered to invert for the slip or creep rate over the fault, which is responsible for the observed GPS and DInSAR horizontal and vertical velocity patterns at the Earth's surface. A purely normal fault-like slip over the Castrovillari fault is assumed in accord with the most updated Database of Individual Seismogenic Sources (DISS Working Group 2007), described in Basili *et al.* (2008), and based on active tectonics data from Cinti *et al.* (2002) as far as the Castrovillari fault is concerned. Fault parameters and geometry are thus characterized by length and width of the fault of 16.0 and 12.0 km, and strike, dip and rake of $157.0°$, $60.0°$ and $270.0°$, respectively; the dip angle of $60.0°$ seems to characterize all the faults in the portion of the southern Apennines portrayed in Fig. 1, from the Melandro-Pergola in the north to the Castiglione-Agri in the south, except for the Luzzi fault, with a dip of $65.0°$. Although there are evidences that rake distribution over the fault can be more complex than a pure normal faulting model (Papanikolaou & Roberts 2007), the lack in literature of a variable rake model for the Castrovillari fault and the dominant extensional

behaviour over the fault suggests us to adopt a simple purely normal faulting mechanism.

In this section, vertical (DInSAR) and horizontal (GPS) constant rates from the linear fit of the data are interpreted in terms of relative motion across the fault of its southwest hanging wall, with respect to the northeast footwall. As for the surface data, this relative motion is constant in time, at least for the time window of surveying, and is thus interpreted in terms of slip or specifically in terms of creep, in analogy with the already known cases of strike-slip Californian and North Anatolian faults. A linear model is thus assumed for both surface data and, consequently, for slip over the fault: more sophisticated non-linear velocity models could be considered in the future, in case of increased time-resolving power of our analysis, in particular in the data set and in specifically designed SAR and GPS data reduction algorithms. A linear velocity model represents in any case the first necessary step towards the appraisal of the new physics of normal fault behaviour brought out by our study.

In the following, a brief description of the inversion scheme, which images creep over the fault from surface velocity data, precedes the results for the two data sets, DInSAR and GPS. Creep
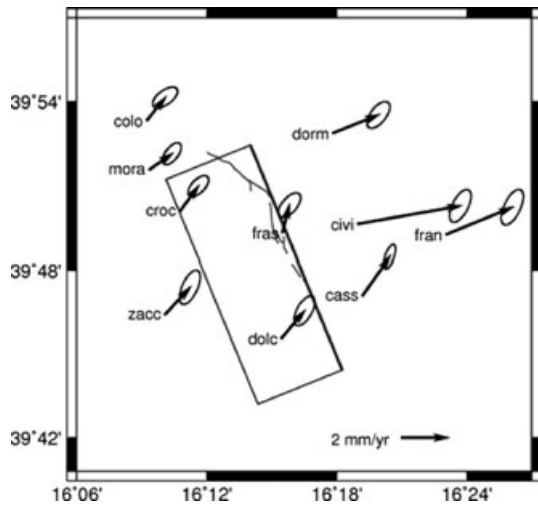
Figure 3. GPS campaign velocities, north (V_N) and east (V_E) components, in the Eurasia reference frame, defined by the geodetic plate kinematic model APKIM2005 and relative 1σ confidence error ellipses (in mm yr^{-1}).

Table 1. GPS campaign velocities and standard deviation (in mm yr^{-1}) in the Eurasia reference frame, defined by the geodetic plate kinematic model APKIM2005.

Sites	V_N	V_E
cass	1.7 ± 0.2	1.2 ± 0.3
civi	0.8 ± 0.3	4.5 ± 0.5
colo	1.0 ± 0.4	0.8 ± 0.3
croc	1.1 ± 0.3	0.8 ± 0.3
dolc	1.2 ± 0.3	1.0 ± 0.4
dorm	0.8 ± 0.3	2.0 ± 0.4
fran	1.2 ± 0.3	2.9 ± 0.5
fras	1.2 ± 0.3	0.3 ± 0.4
mora	0.7 ± 0.3	1.0 ± 0.3
zacc	1.2 ± 0.3	1.1 ± 0.5

over the fault is thus portrayed in terms of slip over the Castrovillari fault, as seen in the perpendicular direction from the western, or Tyrrhenian, side of the fault, which is the subsiding hanging wall.

The fault is subdivided into 192 1 km × 1 km patches (being the reference fault 16 km × 12 km), the slip rate over each patch corresponding to a component of the vector of model unknowns. Surface velocities at the observation points (both DinSAR and GPS) are thus computed as a linear superposition of elementary surface signals due to each patch, calculated on the basis of the forward Okada elastic half-space model (Okada 1992). Inversion is carried out following Occam's inversion method (deGroot-Hedlin & Constable 1990), which states that in the inversion, given an acceptable degree of misfit between modelled results and observed data, the less complex solution has to be chosen. Complexity in solution is measured

Table 2. Strain-rate: E_ min = minimum principal axe; E_max = maximum principal axes.

	nanostrain yr^{-1}	Azimuth (°)
E_min	-54.7 ± 8.6	-15 ± 14
E_max	79.2 ± 35.4	75 ± 14

by means of a roughness term

$$R_0 = \left\| \bar{\partial}_x m \right\|^2 + \left\| \bar{\partial}_y m \right\|^2, \tag{1}$$

where the roughening matrices $\bar{\partial}_x$ and $\bar{\partial}_y$ difference the model parameters between adjacent patches along the strike (x) and dip (y) directions, with m denoting the vector of the slip for each patch. Given this formulation, the functional to be minimized, including the roughening penalization, reads

$$A(m) = \left\| \bar{\partial}_x m \right\|^2 + \left\| \bar{\partial}_y m \right\|^2 + \mu \left\{ \|Wd - WGm\|^2 - X^2 \right\}, \tag{2}$$

where X^2 is the reduced chi-square, W is the weighting diagonal matrix given by the inverses of data uncertainties and G is the Green's function matrix collecting the elementary signals evaluated over each observation point, given by a unit slip rate over each patch.

The average roughness R_0 is varied in the 0.5–1 mm km^{-1} range, which makes the slip pattern over the fault rather smooth, in such a way to avoid localized, probably unrealistically detailed, spots of slip; this roughness is one order of magnitude smaller than the one used for slip pattern due to coseismic displacements (Dalla Via *et al.* 2006), expected to be larger with respect to the creep one. In this perspective, we allow for the possibility of slip-rates different from zero at the fault edges, in full accordance with dislocation theory, which underlies the forward modelling, and with the limited fault dimensions, obtained from active tectonics data.

In Figs 5–10, a detailed analysis of the creep pattern over the fault, separately for DInSAR and GPS inversion, is carried out in terms of roughness and of vertical and horizontal offsets of the whole data sets with respect to the modelled vertical and horizontal surface velocities. Such a detailed discussion of the results enables the reader to capture the intimate nature of fault creep, reaching in particular a deep insight into its variability over the fault surface in terms of data coverage on the Earth's surface.

For DInSAR data, the inversion is overdetermined, since the 192 slip amplitudes over the patches are constrained by the 661 values of the DInSAR vertical displacements plus the roughness conditions among the various patches resulting from the regularization imposed by assuming an upper bound from the allowed average gradient of slip over the fault. Since DInSAR vertical motions are evaluated with respect to an arbitrarily fixed zero, in our case given by an average velocity of four points placed near the centre of the measuring area, as a general rule we are allowed to add a uniform vertical velocity offset, indicated by O$_{fv}$. This offset is chosen in such a way to balance the positive and negative residuals between data and vertical rates obtained from the forward model, within the functional of eq. (1), since the forward model is not likely carrying the same zero vertical velocity used for DInSAR referencing for the case of Fig. 2; this offset can be chosen to minimize the misfit, or the lowest X^2.

Fig. 5 (top panel) shows $R_0 = 1$ mm km^{-1} and O$_{fv} = -2.67$ mm yr^{-1} which minimizes the misfit, the inverted creep rate distribution over the Castrovillari fault for normal-fault like motion using DInSAR velocities portrayed in Fig. 2. The rates are given in millimetres per year, according to the colour scale, over the patches of the fault.

The largest amount of slip is localized in the northernmost (left-hand side) part of the fault from 0 to 7 km along strike, with maximum rates of about 20 mm yr^{-1}, and 24 mm yr^{-1} rates over a limited number of patches, and an average one of 8.5 mm yr^{-1}. From the vertical rate pattern in Fig. 2, it is notable that the large slip rates in the northernmost part of the Castrovillari fault are required to accommodate the large subsidence in the fault's hanging wall, between **mora** and **fras** (Fig. 2). Slip rate is subject to a substantial
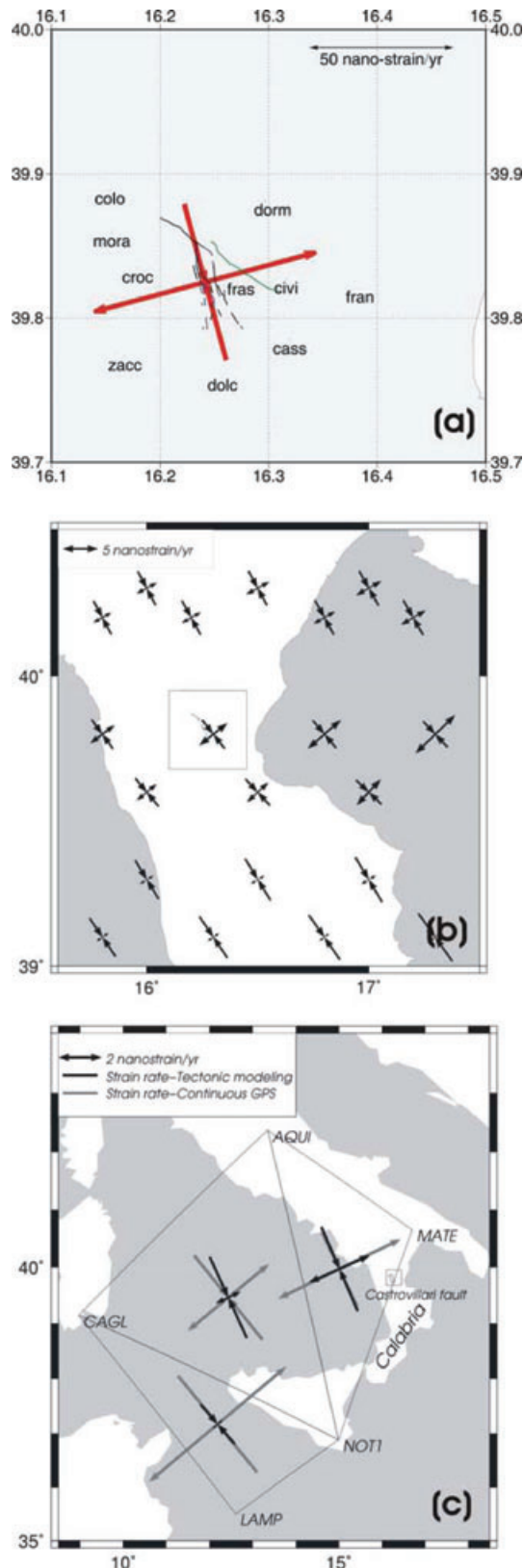
decrease in the half-southern (right-hand side) part of the fault, with a central locked zone.

Creep rates do not vanish at the left and bottom edges of the fault mainly for three reasons: first, we make use of dislocation theory, which allows for displacement discontinuities at the edges; second, by limiting roughness, we smooth the slip over the fault, which leads in turn to slip discontinuities between the fault and its surrounding and, third, we make use of fault dimensions inferred from active tectonics, which could underestimate the creeping surface. In order to show that it is possible to limit slip discontinuities at fault edges we consider in the following (Fig. S4) one more case in which the fault is continued to the north, in such a way to analyse the effects of possible artefacts due to underestimated fault dimension along strike.

The three panels at the bottom of Fig. 5 show the data, including the offset, left-hand panel, the modelled vertical rates at the Earth's surface, central panel and the misfit in the right-hand panel. The average misfit, namely the average of the difference between data and model values at each pixel, is very low, of the order of 0.01 mm yr^{-1} as given by the statistical parameters in the caption; the model reproduces well the data, as indicated by the reduced X^2 lower than unity, although some deviations, of about 1 mm yr^{-1}, remain in the hanging wall. The pattern of vertical rates well reproduces the regions of subsidence and uplift, the former affecting the hanging wall. The model shows the tendency of a sharper transition between subsidence and uplift when compared to the broader pattern from DInSAR analysis in the top left-hand panel. The large slip rates noted above in the top panel in the northern and deepest part of the fault is responsible for the large subsidence (blue) observed in these DInSAR model results and, in conjunction with the locked central sector of the fault, for the smooth uplift (red) in the footwall.

It is possible to reduce the creep rate discontinuity due to dislocation theory at the bottom edge by increasing the offset to -3.6 mm yr^{-1}, as shown in Fig. 6 (top panel). The highest slip rate zone moves upward with respect to the counterpart panel of Fig. 5 remaining in the northern (left-hand panel) part of the fault, which has the effect to reduce the rates at the bottom, thus diminishing the bottom edge effects. Such a large value of the offset has the effect to increase the average misfit to about -0.7 mm yr^{-1}, and increasing the X^2, as given in the caption.

Dealing with vertical modelled velocities, it is notable a global increase of the misfit in the subsiding region and a reduction of residuals in the uplift area (Fig. 6, lower right-hand panel, with respect to its counterpart in Fig. 5), caused by the larger negative vertical offset applied to data, thus fitting better the uplift shown as a light, red spot in the lower right-hand panel of Fig. 6.

Subsidence recorded by DInSAR and resulting from creep modelling is notably concordant with the huge throw along the topographic profile perpendicular to the fault, representing a major

Figure 4. Panel (a) Mean strain-rates (in nanostrain yr^{-1}, corresponding to a change in length of 1 part over 10^9, or 1 mm over 1000 km, for example) from GPS surveying, at the ten GPS sites, **colo** (Coloreto), **croc** (Crocefisso), **dorm** (Dolcedorme), **mora** (Morano), **fras** (Frascineto), **civi** (Civita), **zacc** (Zaccalia), **dolc** (Dolcetti), **cass** (Cassano), **fran** (Francavilla), in the Pollino Range. The thin grey lines indicate the Castrovillari fault scarps

(Cinti *et al.* 2002), attesting its recent activity and where trenches have been opened. The red arrows represent the principal strain-rate axes, converging for compression and diverging for extension. Strain-rate does not include the contribution of **civi** station. Panel (b) Strain rates from thin sheet tectonic (finite element) modelling; the Pollino Range area is indicated by the square, while the Castrovillari fault is indicated by the thin line denoting the fault scarps. Panel (c) strain rate (in nanostrain yr^{-1}, from continuous GPS (grey) and tectonic modelling (black). Converging arrows denote compression and diverging ones extension. Continuous GPS sites are AQUI (Aquila), CAGL (Cagliari), LAMP (Lampedusa), NOT1 (Noto) and MATE (Matera). The thin square zone in Calabria denotes the Pollino Range area, including the Castrovillari fault (small rectangle).
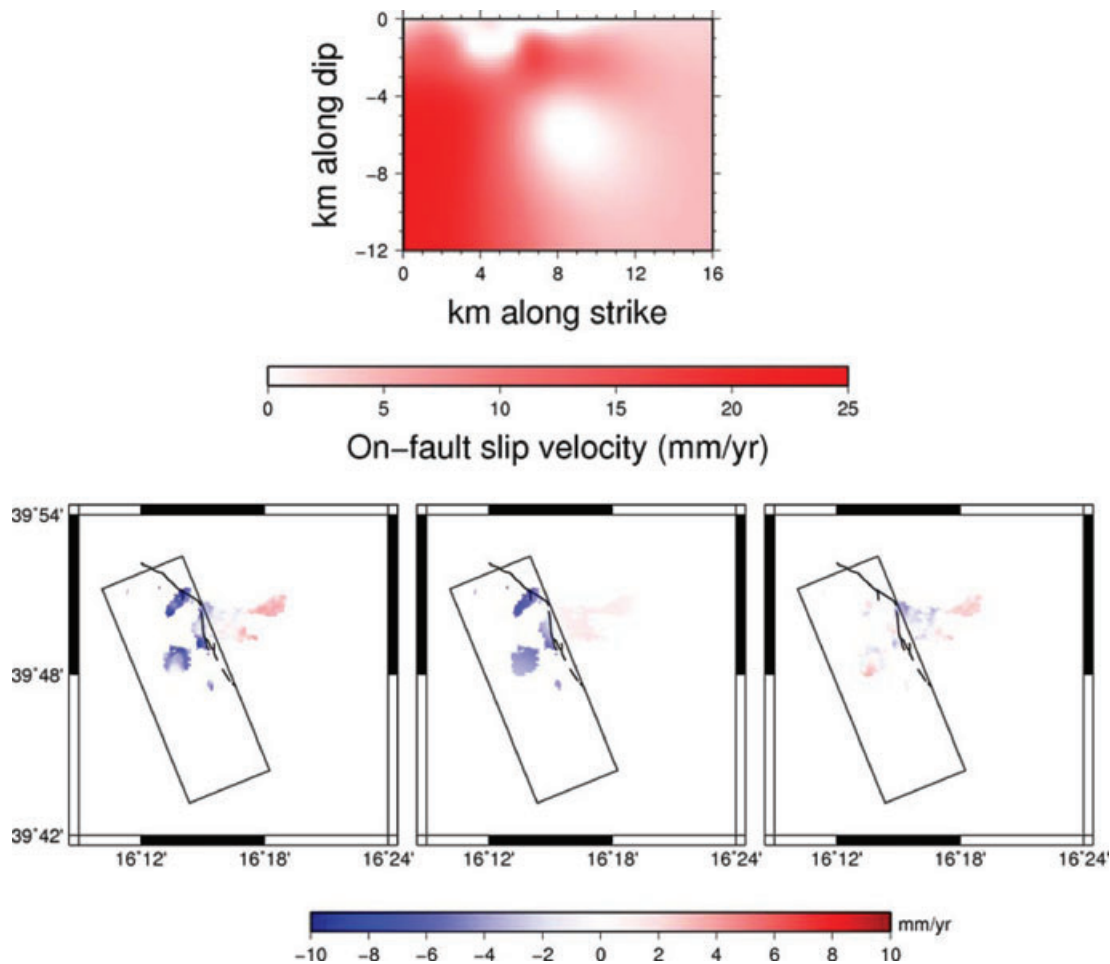
Figure 5. Slip rate over the Castrovillari fault from DInSAR, top panel, with the left-hand border of the fault plane corresponding to its northern edge and the right-hand border to the southern one, as in the following panels. At the bottom panel, DInSAR data including the offset (left-hand panel), model results (centre panel) and misfit (right-hand panel). 16 km × 12 km fault, $R_0 = 1$ mm km^{-1}, $O_{fv} = -2.7$ mm yr^{-1}. Average misfit $= -0.01$ mm yr^{-1}, misfit $SD = 1.9$ mm yr^{-1}, reduced $X^2 = 0.88$, max slip $= 24$ mm yr^{-1}, average slip $= 8.5$ mm yr^{-1}.

geomorphic expression of the active fault system, as shown in Fig. 2 by Cinti *et al.* (2002). Creep thus certainly contributes to surface morphology, although it is difficult to quantify its contribution to elevation changes, being not possible, with the data now at disposal, to precisely define its onset. Our results clearly show that creep, besides coseismic displacement, has to be considered a contributor to surface elevation changes in normal faulting environments.

When the average roughness R_0 is reduced by a factor of 2, as shown in Figs S2 and S3, thus smoothing throughout the fault plane the slip pattern, some amount of slip, of a few millimetres per year at the most, appears also in the southern (right-hand side) part of the fault, although the central part shows the tendency to remain locked.

Edge effects can be reduced also for the left-hand edge of the fault, by increasing along strike to the north (left-hand side) the horizontal dimension of the fault, as shown in Fig. S4, which could account for our uncertainties on fault location.

For GPS inversion, only 20 horizontal displacement components are available, but inversion is well determined by the regularization conditions imposed by assuming an upper bound for the allowed average slip gradient over the fault. Similarly to the vertical offset of the DInSAR case, an horizontal O_{fh} offset, with respect to the geodetic plate kinematic model APKIM2005, is introduced in the

north and east-horizontal displacements, in order to minimize the misfit between GPS data and model predictions, since the zero horizontal displacements assumed for GPS does not necessarily coincide with the zero motion predicted by modelling.

Except for the slip rate spot in the top, right-hand part of the fault, required to accommodate **dolc-cass** relative motion, Fig. 7 shows that GPS is concordant with DInSAR in terms of localization of the largest amount of slip in the northernmost (left-hand panel) part of the fault from 0 to 7 km along strike, with highest rates of about 20 mm yr^{-1}. Differently from DInSAR, slip is not uniformly distributed in depth, but it is rather localized at the top and bottom zones of the northern part of the fault. These slip rates are required by the large extension between **colo**, **mora**, **croc** and **fras** on the hanging wall with respect to **civi, dorm** and **fran** in the footwall, characterizing the normal-fault like pattern of the horizontal motions in the Castrovillari area. The deep creep, at 8–12 km, is required to accommodate the extension between **colo**, **mora**, **croc** with respect to **dorm**, whose distance is comparable with fault dimensions, while the shallow creep in the northern part accommodates the **fras** with respect to **civi, fran** extension, whose distance is smaller than fault dimensions.

The lack of creep at the 4–8 km depth, from GPS inversion differently form DInSAR's one, could thus be ascribed to a
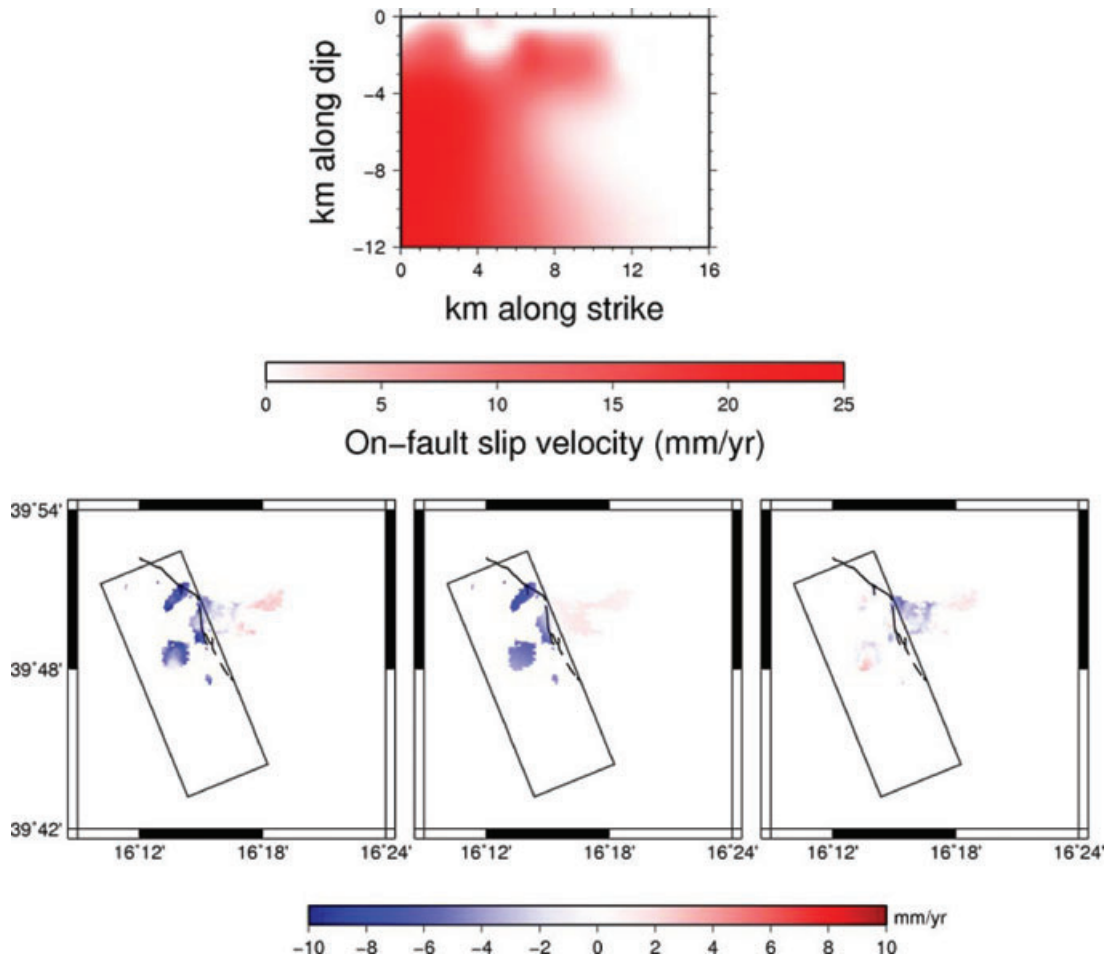
Figure 6. As in Fig. 5, but with offset $O_{fv} = -3.6$ mm yr^{-1}. 16 km $\times$ 12 km fault, $R_0 = 1$ mm km^{-1}, average misfit $= -0.7$ mm yr^{-1}, misfit $SD = 1.9$ mm yr^{-1}, reduced $X^2 = 1.03$, max slip $= 25$ mm yr^{-1}, average slip $= 8$ mm yr^{-1}.
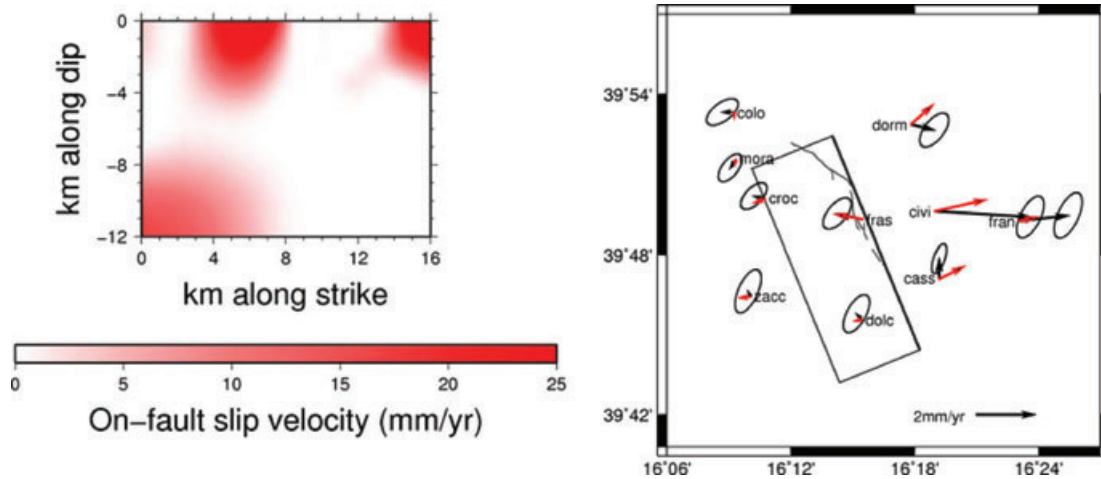

Figure 7. Slip rate over the Castrovillari fault from GPS (left-hand panel). In the right-hand panel, GPS velocities (black arrows), including 1σ error ellipses and modelled ones (red arrows). 16 km $\times$ 12 km fault, $R_0 = 1$ mm km^{-1}, WRT (With Respect To) APKIM2005 (N/E) O_{fh}: $-1.0/-1.2$ mm yr^{-1}, N/E average misfit $= 0.02 / -0.01$ mm yr^{-1}, misfit $SD = 0.6$ mm yr^{-1}, reduced $X^2 = 1.9$, max slip $= 35.3$ mm yr^{-1} average slip $= 3.7$ mm yr^{-1}. Only six patches show a slip larger than 20 mm yr^{-1}.

non-uniform coverage of GPS distribution at the Earth's surface and to incomplete DInSAR data coverage of the surface area overlying the fault.

The slip-rate spot in the southernmost (right-hand panel) part of the fault at 14–16 km along the strike, at the very shallow depth of about 2 km, is required to accommodate the motion between the **cass** and **dolc** sites.

Within the creeping northern part of the fault, GPS in Fig. 7 shows the tendency to focus the highest creep rates at shallow depths with respect to DInSAR, the latter being more uniformly
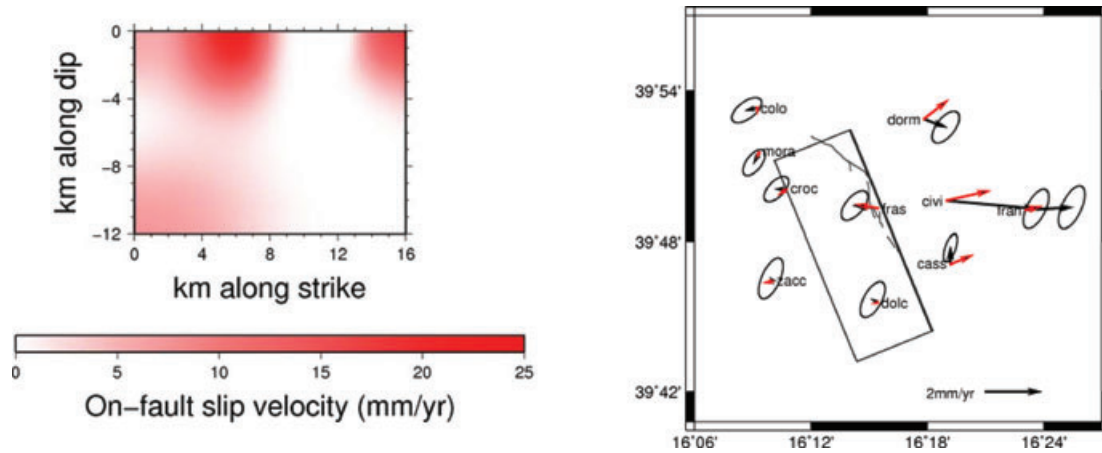
Figure 8. As in Fig. 7. 16 km × 12 km fault but with roughness reduced **to** $R_0 = 0.5$ mm km^{-1}, WRT APKIM2005 (N/E) O$_{fh}$ = $-1.1/-1.2$ mm yr^{-1}, average misfit N/E = 0.03 / -0.03 mm yr^{-1}, misfit SD = 0.6 mm yr^{-1}, reduced X^2 = 2.13, max slip = 20, average slip = 3 mm yr^{-1}.
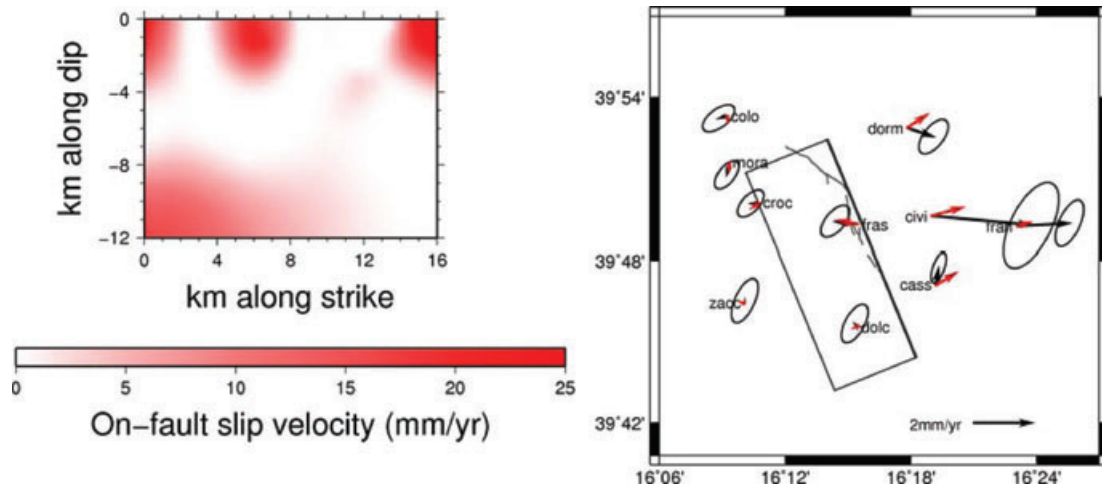
Figure 9. As in Fig. 7. **civi** errors are twice the nominal ones, $R_0 = 1$ mm km^{-1}, O$_{fh}$ WRT APKIM2005 (N/E) : = $-1.1/-1.1$ mm yr^{-1}, average misfit N/E = -0.05 / 0.10 mm yr^{-1}, SD misfit = 0.7 mm yr^{-1}, reduced X^2 = 1.25, max slip = -27.3, average slip = 3.5 mm yr^{-1}. Only one patch shows a slip higher than 20 mm yr^{-1}.
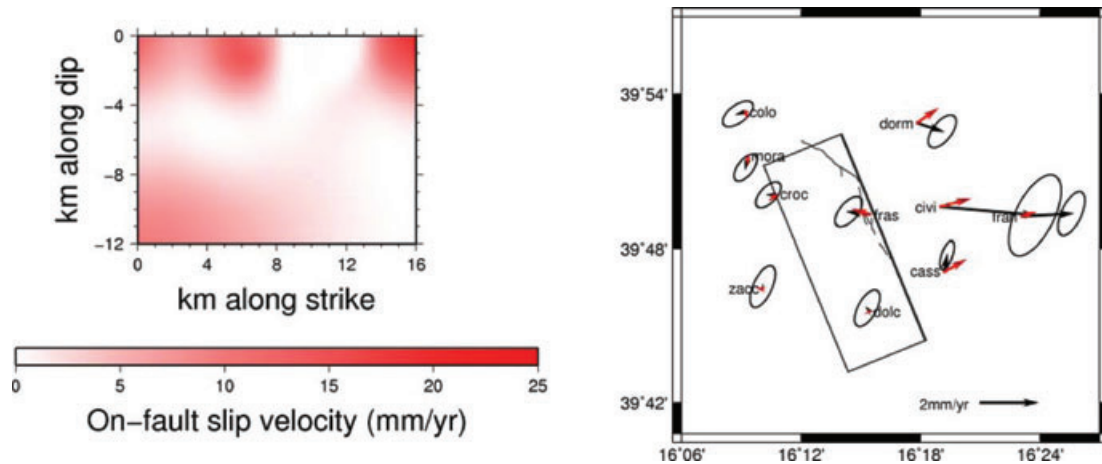

Figure 10. civi errors are twice the nominal ones, $R_0 = 0.5$ mm km^{-1}, O$_{fh}$ WRT APKIM2005 (N/E) = $-1.1/-1.1$ mm yr^{-1}, average misfit N/E = $-0.04/0.08$ mm yr^{-1}, SD misfit = 0.7 mm yr^{-1}, reduced X^2 = 1.33, max slip max = 17.3, average slip = 3.2 mm yr^{-1}.

Table 3. For each GPS site, and for the same parameters of Fig. 7, observed velocity V (corrected for offset), modelled velocity V_m, 1σ measure error, residual and residual weighted by measure error (north and east components).

GPS site	V (mm yr^{-1}) N	E	V_m (mm yr^{-1}) N	E	1σ Err (mm yr^{-1}) N	E	$V - V_m$ (mm yr^{-1}) N	E	$(V - V_m)$/Err N	E
cass	0.7	0.0	0.4	0.9	0.2	0.3	0.3	−0.9	1.5	−2.5
civi	−0.2	3.3	0.4	1.8	0.3	0.5	−0.6	1.5	−1.9	3.2
colo	0.0	−0.4	−0.2	0.0	0.4	0.3	0.2	−0.4	0.6	−1.4
croc	0.1	−0.4	−0.1	−0.4	0.3	0.3	0.2	0.0	0.8	0.0
dolc	0.2	−0.2	0.0	−0.3	0.3	0.4	0.2	0.1	0.8	0.1
dorm	−0.2	0.8	0.7	0.8	0.3	0.4	−0.9	0.0	−2.6	0.1
fran	0.2	1.7	0.2	0.6	0.3	0.5	0.0	1.1	0.1	2.1
fras	0.2	−0.9	0.2	−1.0	0.3	0.4	0.0	0.1	0.1	0.2
mora	−0.3	−0.2	−0.2	0.0	0.3	0.3	−0.1	−0.2	−0.4	−0.5
zacc	0.2	−0.1	0.0	−0.4	0.3	0.5	0.2	0.3	0.7	0.6

Table 4. For each GPS site, and for the same parameters of Fig. 8, observed velocity V (corrected for offset), modelled velocity V_m, 1σ measure error, residual and residual weighted by measure error (north and east components).

GPS site	V (mm yr^{-1}) N	E	V_m (mm yr^{-1}) N	E	1σ Err (mm yr^{-1}) N	E	$V - Vm$ (mm yr^{-1}) N	E	$(V - V_m)$/Err N	E
cass	0.6	0.0	0.3	0.8	0.2	0.3	0.3	−0.8	1.6	−2.3
civi	−0.3	3.3	0.4	1.6	0.3	0.5	−0.7	1.7	−2.1	3.6
colo	−0.1	−0.4	−0.2	0.0	0.4	0.3	0.1	−0.4	0.2	−1.3
croc	0.0	−0.4	−0.2	−0.3	0.3	0.3	0.2	−0.1	0.6	−0.3
dolc	0.1	−0.2	0.0	−0.2	0.3	0.4	0.1	0.0	0.5	−0.1
dorm	−0.3	0.8	0.7	0.9	0.3	0.4	−1.0	−0.1	−3.0	−0.2
fran	0.1	1.7	0.1	0.6	0.3	0.5	0.0	1.1	−0.1	2.2
fras	0.1	−0.9	0.1	−0.8	0.3	0.4	0.0	−0.1	−0.1	−0.2
mora	−0.4	−0.2	−0.2	−0.1	0.3	0.3	−0.2	−0.1	−0.8	−0.3
zacc	0.1	−0.1	−0.1	−0.3	0.3	0.5	0.2	0.2	0.5	0.5

distributed in depth, suggesting a different depth-resolving power from GPS-horizontal and DInSAR-vertical motions; Table 3, for each GPS site, and for the parameters of Fig. 7, provides some detailed statistics of the model, namely the observed velocity V (corrected for offset), modelled velocity V_m, 1σ measure error, residual and residual weighted by measure error (north and east components)

The incomplete coincidence of slip rate patterns from DInSAR and GPS could also be partially ascribed to the different data coverage of GPS and DInSAR data at the Earth's surface. As a matter of fact, there is a spot of subsidence in the vertical DInSAR pattern, which is in fact responsible for some slip in the part of the fault between 8 and 12 km, with respect the locked central and southern parts of the fault, but it is evidently not sufficient to drive the larger slip required by the GPS motion between the **cass** and **dolc** more to the south.

The two techniques are recording fast aseismic creeping within the seismogenic layer with a persistent velocity-weakening locked southern part of the fault for at least a decade, the entire time span covered by the DInSAR and GPS data. It is not possible to establish when creeping started on the fault and a detailed comparison between DInSAR and GPS creep inversions may indicate a different depth-resolving power of the two techniques or an upward migration of creep, the latter suggesting that creep is diminishing, since a smaller number of patches is affected by creep from GPS with respect to DInSAR.

The magnitude of the vectors, except for **civi** and **fran**, is well reproduced within the 1σ ellipses (red arrows), as shown in Fig. 7 (right-hand panel), when the slip rates resulting from the inversion in

Fig. 7 (left-hand panel) are used in the Okada-based forward model to reproduce the surface geodetic deformation. Table 3 provides the details of the measured and modelled velocity components, including some statistics. Azimuths are more severely affected by modelling, particularly at the **dorm**, **cass** sites. It is likely that pure normal faulting does not account for some 3-D aspects of fault creep.

Slip rate is smoothed in Fig. 8, by reducing R_0 to 0.5 mm km^{-1}, and slip now shows the tendency to fill the 4–8 km depth in the northern part of the fault, left-hand panel; Table 4 for each GPS site, and for the same parameters of Fig. 8, provides observed velocity V (corrected for offset), modelled velocity V_m, 1σ measure error, residual and residual weighted by measure error (north and east components).

The right-hand panels of Figs 7 and 8 do not portray significant deviations, except for the improved azimuth of **dolc** of Fig. 8. Maximum slip is severely reduced in Fig. 8, from 35 to 20 mm yr^{-1}, the latter in closer agreement with DInSAR slip rates. Details are given in Table 4. These findings on the 3-D distribution of creep must be taken with caution, due to their sensitivity on roughness and, as observed above, on surface data, DInSAR or GPS, coverage.

The reduced X^2 is large for the two cases of Figs 7 and 8, as seen in their captions: in Figs 9 and 10, detailed in Tables 5 and 6, we show that such large values are due to the **civi** velocity. By considering, as anticipated in the preceding GPS section analysis **civi** velocity eastern component as an outlier, so by using an error twice the nominal one for this site, we substantially reduce the X^2, by a factor of about two; we also considerably reduce maximum slip rates to about 17 mm yr^{-1}, for roughness $R_0 = 0.5$ mm km^{-1},

Table 5. For each GPS site, observed velocity (corrected for offset), modelled velocity, 1σ measure error (for **civi** errors listed are twice the nominal ones), residual and residual weighted by measure error (north and east components), corresponding to Fig. 9.

| GPS site	V (mm yr^{-1}) N	E	V_m (mm yr^{-1}) N	E	1σ Err (mm yr^{-1}) N	E	$V - V_m$ (mm yr^{-1}) N	E	$(V - V_m)$/Err N	E
cass	0.6	0.1	0.4	0.7	0.2	0.3	0.2	−0.6	0.9	−1.8
civi	−0.3	3.4	0.3	1.1	0.6	1.0	−0.6	2.3	−1.0	2.4
colo	−0.1	−0.3	−0.2	0.0	0.4	0.3	0.1	−0.3	0.3	−1.0
croc	0.0	−0.3	−0.2	−0.3	0.3	0.3	0.2	0.0	0.5	−0.1
dolc	0.1	−0.1	−0.1	−0.1	0.3	0.4	0.2	0.0	0.5	0.1
dorm	−0.3	0.9	0.5	0.7	0.3	0.4	−0.8	0.2	−2.3	0.5
fran	0.1	1.8	0.1	0.5	0.3	0.5	0.0	1.3	−0.1	2.5
fras	0.1	−0.8	0.1	−0.7	0.3	0.4	0.0	−0.1	−0.1	−0.2
mora	−0.4	−0.1	−0.2	0.0	0.3	0.3	−0.2	−0.1	−0.7	−0.2
zacc	0.1	0.0	0.1	−0.2	0.3	0.5	0.0	0.2	0.1	0.4

Table 6. For each GPS site, observed velocity (corrected for offset), modelled velocity, 1σ measure error (for **civi** error listed are twice the nominal ones), residual and residual weighted by measure error (north and east components), corresponding to Fig. 10.

GPS site	V (mm yr^{-1}) N	E	V_m (mm yr^{-1}) N	E	1σ Err (mm yr^{-1}) N	E	$V - V_m$ (mm yr^{-1}) N	E	$(V - V_m)$/Err N	E
cass	0.6	0.1	0.4	0.7	0.2	0.3	0.2	−0.6	1.1	−1.8
civi	−0.3	3.4	0.3	1.0	0.6	1.0	−0.6	2.4	−0.9	2.5
colo	−0.1	−0.3	−0.2	0.0	0.4	0.3	0.1	−0.3	0.2	−1.0
croc	0.0	−0.3	−0.2	−0.2	0.3	0.3	0.2	−0.1	0.6	−0.2
dolc	0.1	−0.1	0.0	−0.1	0.3	0.4	0.1	0.0	0.5	0.0
dorm	−0.3	0.9	0.5	0.7	0.3	0.4	−0.8	0.2	−2.4	0.5
fran	0.1	1.8	0.1	0.5	0.3	0.5	0.0	1.3	−0.1	2.6
fras	0.1	−0.8	0.2	−0.6	0.3	0.4	−0.1	−0.2	−0.3	−0.6
mora	−0.4	−0.1	−0.2	0.0	0.3	0.3	−0.2	−0.1	−0.8	−0.2
zacc	0.1	0.0	0.0	−0.2	0.3	0.5	0.1	0.2	0.2	0.3

without substantially affecting the patterns of horizontal motions depicted in the right-hand panels of Figs 9 and 10 with respect to their counterparts of Figs 7 and 8.

Although the dip angle is fixed at 60.0° in the most updated literature, two extreme cases of dip angles of 40.0° and 70.0° are also tested and shown in Figs S5 and S6. Except for a general deterioration of the misfit, as revealed by the higher X^2 values for GPS inversion, the creep rate pattern remains rather stable with respect to the previous findings for the 60.0° dip case, suggesting that the latter obtained from palaeoseismology is well in agreement with a totally different class of data, namely the geodetic ones. Since the lower dip of 40.0° is more efficient in driving subsidence over a wider area of the Earth's surface with respect to the higher dip angles, lower creep rates are required by DInSAR inversion for such a shallow dip with respect to the ones for 60.0° and 70.0°.

The reduced X^2, as a function of the roughness R_0, is shown in Fig. 11, varying from 0.1 to 2.5 mm yr^{-1}. Although increasing the roughness would help to reduce the misfit, by making the fit of the data easier thanks to the larger slip gradients over the fault, roughness should be chosen as low as possible, in agreement with the Occam type inversion scheme which favours the smoothest slip models. This figure shows that our choice for R_0 in the range 0.5–1.0 mm yr^{-1} represents a good compromise, which guarantees the smoothest slip and a X^2 value reasonably close to the limit attained by large R_0. Our choices are particularly appropriate for DInSAR data, being larger in number with respect to GPS ones, thus attaining, in general, lower X^2. It is notable that,
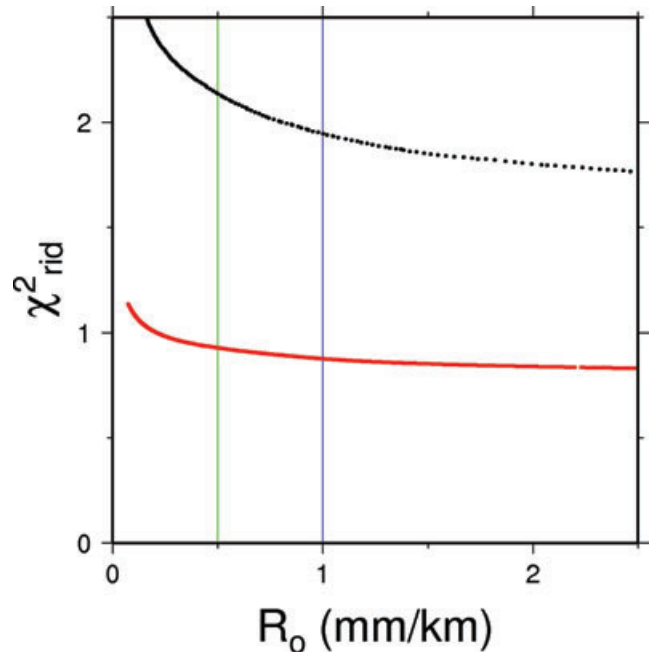
Figure 11. Reduced X^2 as a function of roughness R_0, red for DinSAR and black for GPS. The green and blue vertical lines denote the roughness values considered in our analysis.

despite the fact that maximum slip rates are strongly affected by the choice of allowed roughness level, the average slip rates are rather stable.

5 CONCLUSIONS

The combined use of DInSAR and GPS data has made it possible to capture the first evidences of fast creeping over a normal fault in the Mediterranean, during the interseismic phase of the Castrovillari fault. Creep occurs over all depths of the seismogenic layer and is embedded in a generally slowly deforming zone. The velocity-strengthening creeping zone reaches maximum rates of the order 20 mm yr^{-1}, within an average background of 3–9 mm yr^{-1}, and limits to the north a velocity-weakening southern part from which an earthquake could depart: these rates are higher than the average slip rate of 1 mm yr^{-1} of the Castrovillari fault from palaeoseismology (Cinti *et al.* 2002), suggesting that we are detecting a fast transient. The creep rates are comparable instead with those along the (strike-slip) North Anatolian fault (NAF; Ambraseys 1970; Cakir *et al.* 2005): this phenomenon was discovered for the San Andreas fault in California (Steinbrugge *et al.* 1960), where DInSAR techniques has been successfully applied to analyse fault creep along the San Andreas, Calaveras and Hayard faults (Bürgmann *et al.* 1998, 2000; Rosen *et al.* 1998) but the novelty of our results is that creep is now first evidenced and proven to be feasible also for normal faulting.

Although the onset of creep over the Castrovillari fault cannot be established, creep over there is a long-lasting phenomenon, of at least one decade, the time-interval covered by DInSAR-GPS data: such a timescale is suggested herein to characterize transient phenomena for normal-faulting, which seems to be feasible for strike-slip environments also, as those detected by Cakir *et al.* (2005) along the NAF. This decade creep seems in fact to reflect another similarity with the strike-slip faults, since the former over the NAF has also been observed to be long-lasting, over decades (Cakir *et al.* 2005). The GPS average creep rates, smaller by a factor of two with respect to DInSAR ones, could reflect their different surface data coverage or an overall reduction in the intensity of the phenomenon in the last few years of GPS measurements.

Our results are thus of importance for establishing that creep is a general rule for active faults, not limited to strike-slip environments. They also shed light on the mode in which deformation is distributed among the various parts of the whole seismogenic zone or single fault, which has of course implications on the pattern of stress-built up and thus earthquake generation.

The fault standing right at the geological transition between the Southern Apennines and the Calabrian Arc exhibits different geological sequences on its two sides (Bousquet 1973). This may create unusually high pore pressures in the fault zone as a result of metamorphic fluids being exuded from one side and capped by the other. Studies of the Earth's structure beneath the Castrovillari–Pollino zone report a slab window with sideways asthenospheric flow (Gvirtzman & Nur 1999; Panza *et al.* 2007), which would enhance fluid circulation. In these two complementary interpretations, overpressurization would result in low effective normal stress on the fault and, hence, narrow the unstable patches on it. There are numerous important reasons for engaging in detailed studies of the aseismic deformation on seismogenic faults. Aseismic slip can exert a strong influence on the moment budget of faults, which needs to be quantified for accurate seismic hazard estimates. Aseismic slip also redistributes stress in the crust, thereby affecting the locations of future earthquakes. Finally, imaging aseismic slip may help to constrain constitutive laws of fault zones (Han *et al.* 1999; Moore & Rymer 2007).

REFERENCES

Ambraseys, N.N., 1970. Some characteristic features of the Anatolian fault zone, *Tectonophysics,* **9,** 143–165.

Amiri-Simkooei, A.R., 2007. Least-squares variance component estimation: theory and GPS applications, *PhD thesis.* Vol. 64, Delft University of Technology, Publication on Geodesy, Netherlands Geodetic Commission, Delft.

Basili, R., Valensise, G., Vannoli, P., Burrato, P., Fracassi, U., Mariano, S., Tiberti, M.M. & Boschi, E., 2008. The Database of Individual Seismogenic Sources (DISS), version 3: summarizing 20 years of research on Italy's earthquake geology, *Tectonophysics,* **453,** 20–40, doi:10.1016/j.tecto.2007.04.014.

Battaglia, M., Murray, M.H., Serpelloni, E. & Bürgmann, R., 2004. The Adriatic region: an independent microplate within the Africa-Eurasia collision zone, *Geophys. Res. Lett.,* **31**(9), L09605, doi:10.1029/2004GL019723.

Biescas, E., Crosetto, M., Agudo, M., Monserrat, O. & Crippa, B., 2007. Two Radar Interferometric approaches to monitor slow and fast land deformation, *J. Surv. Eng.,* **133,** 66–71.

Bousquet, J.C., 1973. La tectonique récente de l'Apennin Calabro-Lucanien dans son cadre géologique et géophysique, *Geol. Rom.*, **12,** 1–103.

Bürgmann, R., Fielding, E. & Sukhatme, J., 1998. Slip along the Hayward fault, California, estimated from space-based synthetic aperture radar interferometry, *Geology,* **26**(6), 559–562.

Bürgmann, R., Schmidt, D., Nadeau, R.M., d'Alessio, M., Fielding, E., Manaker, D., McEvilly, T.V. & Murray, M.H., 2000. Earthquake potential along the northern Hayward Fault, California, *Science,* **289,** 1178–1182.

Cakir, Z., Akoglu, A.M., Belabbes, S., Ergintav, S. & Meghraoui, M., 2005. Creeping along the Ismetpasa section of the North Anatolian fault (Western Turkey): rate and extent from InSAR, *Earth planet. Sci. Lett.,* **238,** 225–234.

Camassi, R. & Stucchi, M., NT4.1, 1997. A parametric catalogue of damaging earthquakes in the Italian area (release NT4.1.1), G.N.D.T., Milano, XXVII, pp. 66. (http://emidius.itim.mi.cnr.it/NT/home.html).

Cinti, F.R., Moro, M., Pantosti, D., Cucci, L. & D'Addezio, G., 2002. New constraints on the seismic history of the Castrovillari fault in the Pollino gap (Calabria, southern Italy), *J. Seismol.,* **6,** 199–217.

Dach, R., Hugentobler, U., Fridez, P. & Meindl, M., 2007. Bernese GPS Software Version 5.0, Astronomical Institute, University of Bern.

Dalla Via, G., Crippa, B., Toraldo Serra, E.M., Giacomuzzi, G. & Sabadini, R., 2006. Exploitation of high-density dinsar data points of the um-bria_marche (Italy) 1997 seismic sequence for fault characteristics, *Geophys. Res. Lett.,* **34,** L17301, doi:10.1029/2007GL030718.

deGroot-Hedlin, C. & Constable, S., 1990. Occam's inversion to generate smooth, two dimensional models from magnetotelluric data, *Geophysics,* **55,** 1613–1624.

DISS Working Group, (2007). Database of Individual Seismogenic Sources (DISS), Version 3.0.4: a compilation of potential sources for earthquakes larger than M 5.5 in Italy and surrounding areas, http://www.ingv.it/DISS/, © INGV 2007-Istituto Nazionale di Geofisica e Vulcanologia-All rights reserved.

Drewes, H., 2006. The APKIM2005, basis for a non-rotating ITRF, International IAG Symposium "Geodetic Reference Frames, GRF2006", LVG, München, 2006–10-11 [http://129.187.165.2/fileadmin/platemotions/].

Gvirtzman, Z. & Nur, A., 1999. The formation of Mount Etna as a consequence of slab roll-back, *Nature,* **401,** 782–785.

Han, R., Shimamoto, T., Hirose, T., Ree, J. & Ando, J., 1999. ultralow friction of carbonate faults caused by thermal decomposition, *Science,* **316,** 878–881.

Hugenobler, U. *et al*., 2000. CODE IGS Analysis Center Technical Report.

ITRF2005, http://lareg.ensg.ign.fr/ITRF_solutions/2005//ITRF2005.php

Marotta, A.M. & Sabadini, R., 2004. The signatures of tectonics and glacial isostatic adjustment revealed by the strain rate in Europe, *Geophys. J. Int.,* **157,** 865–870.

Marotta, A.M., Mitrovica, J.X., Sabadini, R. & Milne, G., 2004. The signatures of tectonics and glacial isostatic adjustment revealed by the strain rate in Europe, *J. geophys. Res.,* **109,** B01413, doi:10.1029/2002JB002337.

Moore, D.E. & Rymer, M.J., 2007. Talc-bearing serpentinite and the creeping section of the San Andreas fault, *Nature,* **448,** 795–497.

Nikolaidis, R., 2002. Observation of Geodetic and Seismic Deformation with the Global Positioning System, *PhD thesis*. University of California, San Diego.

Okada, Y., 1992. Internal deformation due to shear and tensile faults in a half-space. *Bull. seism. Soc. Am.,* **82,** 1018–1040.

Panza, G.F., Peccerillo, A., Aoudia, A. & Farina, B., 2007. Geophysical and petrological modeling of the structure and composition of the crust and upper mantle in complex geodynamic settings: the Tyrrhenian sea and surroundings, *Earth Sci. Rev.,* **80,** 1–46.

Papanikolaou, I.D. & Roberts, G.P., 2007. Geometry, kinematics and deformation rates along the active normal fault system in the southern Apennines: implications for fault growth, *J. Struct. Geol.,* **29,** 166–188.

Rosen, P., Werner, C., Fielding, E., Hensley, S., Buckley, S. & Vincent, P., 1998. Aseismic creep along the San Andreas fault northwest of Parkfield, CA measured by radar interferometry, *J. geophys. Res.,* **25,** 825–828.

Steinbrugge, K.V., Zacher, E.G., Tocher, D., Whitten, C.A. & Clair, C.N., 1960. Creep on the San Andreas fault, *Bull. seism. Soc. Am.,* **50,** 396–404.

Widowinski, S., Bock, Y., Zhang, J., Fang, P. & Genrich, J., 1997. Southern California Permanent GPS Geodetic Array: spatial filtering of daily positions for estimating coseismic and postseismic displacements induced by the 1992 Landers earthquake, *J. geophys. Res.,* **102**(B8), 18 057–18 070.

Wright, T.J., Parsons, B.E. & Lu, Z., 2004. Toward mapping surface deformation in three dimensions using InSAR, *Geophys. Res. Lett.,* **31,** L01607, doi:10.1029/2003GL018827.

SUPPORTING INFORMATION

Additional Supporting Information may be found in the online version of this article:

Supplement S1. This supplementary file contains Tables S1–S3 and Figs S1–S6.

Please note: Wiley-Blackwell are not responsible for the content or functionality of any supporting materials supplied by the authors. Any queries (other than missing material) should be directed to the corresponding author for the article.